Available online at www.sciencedirect.com

SciVerse ScienceDirect

Geochimica et Cosmochimica Acta 91 (2012) 271–282

Geochimica et Cosmochimica Acta

www.elsevier.com/locate/gca

Reaction of water-saturated supercritical CO_2 with forsterite: Evidence for magnesite formation at low temperatures

Andrew R. Felmy *, Odeta Qafoku, Bruce W. Arey, Jian Zhi Hu, Mary Hu, H. Todd Schaef, Eugene S. Ilton, Nancy J. Hess, Carolyn I. Pearce, Ju Feng, Kevin M. Rosso

Pacific Northwest National Laboratory, P.O. Box 999, MS K8-96, Richland, WA 99352, USA

Received 16 August 2011; accepted in revised form 30 May 2012; available online 13 June 2012

Abstract

The nature of the reaction products that form on the surfaces of nanometer-sized forsterite particles during reaction with H_2O-saturated supercritical CO_2 ($scCO_2$) at 35 °C and 50 °C were examined under in situ conditions and ex situ following reaction. The in situ analysis was conducted by X-ray diffraction (XRD). Ex situ analysis consisted of scanning electron microscopy (SEM) examination of the surface phases and chemical characterization of precipitates using a combination of confocal Raman spectroscopy, ^{13}C and ^{29}Si NMR spectroscopy, and energy-dispersive X-ray spectroscopy (EDS). The results show that the forsterite surface is highly reactive with the primary reaction products being a mixture of nesquehonite ($MgCO_3 \cdot 3H_2O$) and magnesite ($MgCO_3$) at short reaction times (~3–4 days) and then magnesite ($MgCO_3$) and a highly porous amorphous silica phase at longer reaction times (14 days). After 14 days of reaction most of the original forsterite transformed to reaction products. Importantly, the formation of magnesite was observed at temperatures much lower (35 °C) than previously thought needed to overcome its well-known sluggish precipitation kinetics. The conversion of nesquehonite to magnesite liberates H_2O which can potentially facilitate further metal carbonation, as postulated by previous investigators, based upon studies at higher temperature (80 °C). The observation that magnesite can form at lower temperatures implies that water recycling may also be important in determining the rate and extent of mineral carbonation in a wide range of potential CO_2 storage reservoirs.

1. INTRODUCTION

Capture and storage of carbon dioxide in deep geologic formations represents one of the most promising options for helping mitigate the impacts of greenhouse gases on global warming, owing to the potentially large capacity of these formations and their broad regional availability (Bachu, 2002, 2008; Bachu and Adams, 2003; Benson and Surles, 2006). Mineral–fluid interactions are of prime importance for reservoir permanence through prospective carbonation reactions that trap CO_2 in the form of mineral phases such as metal carbonates (Kaszuba et al., 2003, 2005; Pruess et al., 2003; Suto et al., 2007; Xu et al., 2007). As a result, several investigators have examined the reactivity of aqueous solutions in contact with $scCO_2$ with different mineral phases including portlandite, anorthite, wollastonite, and olivine (Giammar et al., 2005; Regnault et al., 2005; Hanchen et al., 2006; Lin et al., 2008; Prigiobbe et al., 2009; Garcia et al., 2010; King et al., 2010; Daval et al., 2011; Guyot et al., 2011). These studies have shown that the primary reaction products are divalent metal carbonates (e.g., calcite and magnesite) and, for the initial phases containing silica, either amorphous silica or at least a mineral surface enriched in silica.

* Corresponding author. Tel.: +1 509 371 6356; fax: +1 509 371 6354.

E-mail address: ar.felmy@pnnl.gov (A.R. Felmy).

0016-7037/$ - see front matter © 2012 Published by Elsevier Ltd.
http://dx.doi.org/10.1016/j.gca.2012.05.026

Unique conditions for metal carbonation are created in the low water environments associated with subsurface injection of $scCO_2$, such as where the buoyant $scCO_2$ plume progressively displaces formation fluid at the interface with overlying caprock (Nordbotten and Celia, 2006) as well as near field to the injection point. Indeed, recent laboratory work has shown that reactions between water-containing $scCO_2$, or "wet" $scCO_2$, and alkaline earth silicates leads to rapid formation of carbonate minerals (Regnault et al., 2005; Lin et al., 2008; McGrail et al., 2009; Kwak et al., 2010, 2011; Loring et al., 2011), despite the fact that the solubility of water in $scCO_2$ is very small (~0.4%) under these conditions (Spycher et al., 2003). In particular, Kwak et al. (2011), in a study of the interaction of forsterite with variably wet $scCO_2$, showed that at or above saturation of H_2O in $scCO_2$, the dominant end product switched from hydrated/hydroxylated Mg-carbonates (HHMC) and silica species to magnesite and amorphous silica, a process that effectively liberates H_2O and marked the transition between H_2O acting as reactant versus catalyst. For example, if nesquehonite is initially formed by the reaction of wet $scCO_2$ with forsterite,

$$Mg_2SiO_4 + 2CO_2 + 6H_2O \rightarrow 2MgCO_3 \cdot 3H_2O\,(\text{nesquehonite}) \quad (1)$$

Later decomposition to anhydrous magnesite

$$MgCO_3.3H_2O \rightarrow MgCO_3\,(\text{magnesite}) + 3H_2O \quad (2)$$

liberates water. It was proposed that the net effect of this transition was to enhance the rate and extent of reaction. Although the study demonstrated a path to facile magnesite formation, the experiments were limited to a temperature of 80 °C.

Many potentially important geologic CO_2 disposal reservoirs have much lower temperatures. For example, formations containing oil reservoirs are generally at much lower temperatures (20–80 °C; Suto et al., 2007), and many deep saline aquifers also show temperatures at or below 80 °C. For example, McPherson (2006) showed that 14 out of 25 potential CO_2 disposal sites in deep saline aquifers in Colorado USA were at or below 80 °C (McPherson, 2006). Consequently, it is of interest to examine if the mineral reactivity observed at these higher temperatures also occurs at lower temperatures (<80 °C). The challenge in doing so is that the metal carbonation process is expectedly much slower at lower temperatures and therefore harder to probe on laboratory time-scales. This includes much slower dissolution rates of primary silicates, the source of divalent cations needed to form metal carbonate products, and potentially much slower nucleation and growth of the metal carbonates. An important example of the latter is the well-known sluggish precipitation of magnesite (Hanchen et al., 2008; Saldi et al., 2009). Kinetic constrains to magnesite formation have been thought to be linked to the high dehydration energy of Mg^{2+} (Saldi et al., 2009). In fact, to the best of our knowledge there has been only one other reported case of magnesite formation at temperatures between 40 °C and 50 °C (Deelman, 1999), but in this case it required cycling the pH of a ~0.9 M NaCl solution containing $MgCl_2$, $MgSO_4$, and $CaCO_3$ 14 times between pH 5.3 and 8.85 via loss or gain of CO_2 and heating to 50 °C. As pointed out by Saldi et al. (2009), the issue of understanding the precipitation of magnesite is one that may prove pivotal in the development of efficient carbon sequestration techniques. Hence, fundamental questions about metal carbonate reactivity at low temperatures are both highly relevant and remain largely unaddressed.

Here we characterize the metal carbonation reactions of forsterite exposed to H_2O-saturated $scCO_2$ at the relatively low temperatures of 35 °C and 50 °C using a combination of ex situ techniques including scanning electron microscopy and energy-dispersive spectroscopy (SEM/EDS), confocal Raman spectroscopy, ^{13}C and ^{29}Si nuclear magnetic resonance (NMR) spectroscopy; as well as in situ X-ray diffraction (XRD). To help overcome the sluggishness of reactions at low temperatures, the study was conducted using nano-size forsterite which, because of its large surface area/gram, facilitated the formation and hence observation of reaction products at lower temperatures and at a time-scale accessible to both in situ and ex situ measurements.

2. EXPERIMENTAL METHODS

The forsterite was prepared by the procedure of Chen and Navrotsky (2010) and Saberi et al. (2007) using an aqueous solution of magnesium nitrate ($Mg(NO_3)_2{\cdot}6H_2O$), 0.0142 mol, sucrose (0.0568 mol), and colloidal silica (0.0071 mol, 14 nm particle size) at a MgO/SiO_2 molar ratio of 2 (Saberi et al., 2007; Chen and Navrotsky, 2010). This mixture was reacted with stirring for 2 h followed by the addition of polyvinyl alcohol (PVA) (0.0071 mol) in deionized distilled (DDI) water (20 ml). The pH was adjusted to 1 by addition of dilute nitric acid and mixing was continued for 4 h at 80 °C. The solution was then boiled for complete dehydration, converting to a viscous dark-brown gel then to a black foamed mass. The mass was ground into powder and calcined in a furnace at 850 °C for 3 h to form a white powder of forsterite. The BET surface area of the forsterite was 11.8 m^2/g. XPS analysis yielded a Mg:Si ratio of 2.03 indicating little surface enrichment. XRD analysis of the prepared material showed the presence of crystalline forsterite, along with a small amount (<2%) of MgO (Fig. 1). Refinement of the cell model using TOPAS (Bruker Scientific) software indicated an average crystallite size of 63 nm. This approximate crystallite size is also in good agreement with SEM images of the starting material, Fig. 2, which shows individual particles with crystallite sizes varying between approximately 50 and 100 nm.

The reactivity studies were conducted in stainless steel vessels (Model 4790, Parr Instrument Company) with a net volume of approximately 33 cm^3. Each reaction vessel was loaded with stainless steel vials containing 0.05 g of the synthetic forsterite. The vials were open to the $scCO_2$ phase. A controlled amount of DDI was then added to the reaction vessel using a micro-pipette prior to pressurizing the vessel. This procedure allowed the water to dissolve into the $scCO_2$ but prevented any liquid water from contacting the nanoforsterite. The amount of added water (0.5 g) was sufficient to maintain water saturation of the $scCO_2$ under all reaction conditions (i.e. 35 °C, 50 °C and

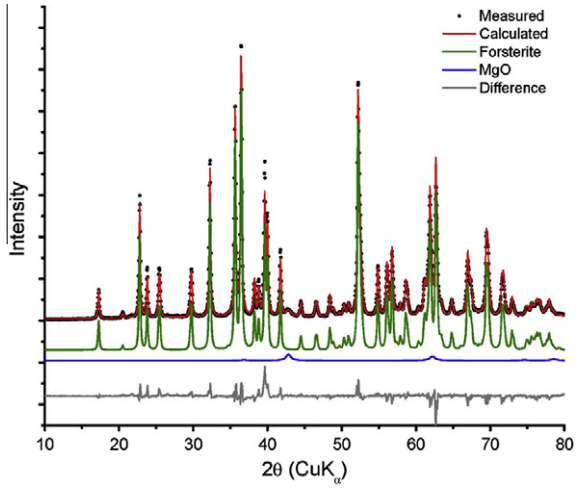

Fig. 1. XRD pattern for the nanoforsterite starting material. The material is crystalline forsterite with the possible presence of a small amount of MgO.

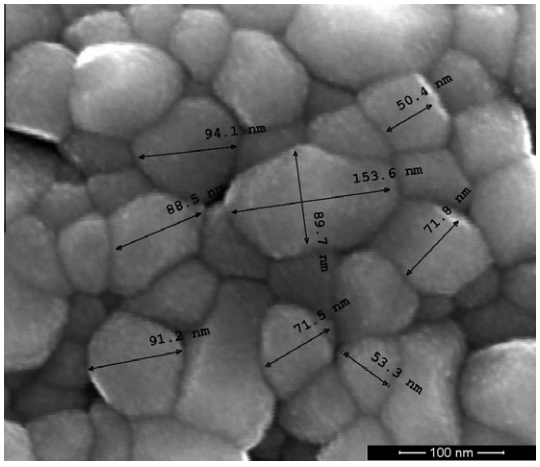

Fig. 2. SEM images of the unreacted nanoforsterite showing the different individual particles and their approximate dimensions.

90 atm (9 Mpa) pressure; Spycher et al., 2003). The standard volumetric adsorption method was then employed to load a controlled amount of ^{13}C labeled, $^{13}CO_2$, into the reactor. This was done by condensing 150 cm^3 of CO_2 at 5.5 atm (0.55 Mpa) several times into the reactor using liquid nitrogen cooling, similar to procedure described by Kwak et al. (2010). The CO_2 transfer corresponded to an initial CO_2 mass of approximately 20 g (estimated CO_2 density of 0.6501 g cm^{-3}) at 35 °C and approximately 9 g (estimated CO_2 density of 0.2906 g cm^{-3}) at 50 °C (Angus et al., 1976). This mass of CO_2 yielded a CO_2 pressure of 90 atm at corresponding 35 °C and 50 °C temperatures as measured by a pressure sensor within the reaction vessel. At the end of the reaction, the experiments were quenched to room temperature and pressure and then examined by ex situ analysis.

In situ XRD experiments were conducted in a high pressure X-ray diffraction reactor, previously described in Schaef et al. (2011, 2012) in order to examine forsterite reactivity at pressure and temperature. The reactor consists of a stainless steel base, small Kapton pockets, and a beryllium cap that is pressure rated up to 200 bars. Small amounts of powdered (~2 mg) sample were pressed into the sample pocket with a glass slide. Water (40 μl) was then added to the bottom of the reactor, not in contact with the sample, sufficient to maintain constant water saturation with the total added CO_2 (2.4–3.2 g) at the temperatures and pressures studied (Spycher et al., 2003). The pocket was attached to the base with a small flat head screw and placed on a custom built XYZ environmental stage attached to a Bruker-AXS D8 Discover XRD unit equipped with a rotating Cu anode (1.54 Å), göbel mirror, 0.5 mm collimator, and 0.5 mm pin hole (Madison, WI). Patterns were collected with a GADDS® area detector positioned at 28.0° 2θ with a measured distance from the sample of 15 cm. Collection of individual XRD tracings required 200 s with power settings of 45 kV and 200–250 mA. Images were processed with Bruker-AXS GADDS® software before importing into JADE® XRD software to obtain peak positions and intensities, reported in °2θ. X-ray diffraction identification was based on reflections reported on the JCPDS cards 20-0669 (nesquehonite), 7-0074 (forsterite), and 8-0479 (magnesite).

Both ^{29}Si and ^{13}C magic angle spinning (MAS) experiments were performed on a Varian-Chemagnetics 300 MHz Infinity spectrometer, corresponding to ^{1}H, ^{13}C and ^{29}Si Larmor frequencies of 299.98, 75.43, and 59.59 MHz, respectively. A commercial cross-polarization/MAS probe with a 7.5 mm outside diameter and 6 mm internal diameter pencil type spinner system was used. The sample cell resembles the commercial cell except that two solid Teflon plugs were made in such a manner that they can only be fully inserted into the zirconium cylinder after pre-cooling using liquid nitrogen to seal about 59.2 mg (reacted at 35 °C) and 74.2 mg (reacted at 50 °C) samples inside the rotor. High power ^{1}H decoupling with a decoupling field strength of approximately 50 kHz was used for acquiring both ^{29}Si and ^{13}C MAS NMR spectra. The sample spinning rate used for all the measurements was about 6.0 kHz. Tetrakis(trimethylsilyl) silane (TKS), $[(CH_3)_3Si]_4Si$, was used as the secondary references for ^{13}C (3.5 ppm) and ^{29}Si (−9.8 ppm) relative to TMS (0 ppm for both ^{13}C and ^{29}Si), (Hayashi and Hayamizu, 1991). The pulse angle for acquiring both ^{13}C and ^{29}Si spectra was approximately 45°. The recycle times used were 5 s for ^{13}C single pulse (SP) experiment and 20 s for ^{29}Si SP, respectively, while 5 s was used for ^{1}H–^{13}C CP using a contact time of 4 ms. All the spectra were acquired at room temperature.

Quantitative peak areas for the peaks with different chemical shifts in either ^{13}C SP-MAS, or ^{29}Si SP-MAS NMR spectra were obtained using the following strategy. The weight of the samples loaded into the MAS rotor for each sample was recorded during sample loading. The matching and tuning conditions of the RF circuit of the probe were set the same using a network analyzer. All other experimental conditions were kept identical from sample to sample. In this way, the absolute peak area against the

spectrometer standard is directly proportional to the sample weight and the number of accumulation numbers. Spectral deconvolution of overlapping peaks was performed using NutsPro (Acorn NMR, 1993–1997), a commercially available software package. The peak area obtained from NutsPro was then normalized based on per unit weight of samples and per unit number of accumulation numbers. The normalized peak area can then be quantitatively compared between the samples.

Raman spectra of the reacted forsterite powders were collected following the NMR experiments on an inverted Raman confocal microscope with automated *xy* mapping stage. A few milligrams of the reacted forsterite powders were dispersed on a glass slide and imaged using a video camera. For Raman measurements on the inverted microscope approximately 2–20 mW of 514.0 nm excitation from a CW Nd:YAG diode laser was focused with a 100× objective to an approximate 1 μm spot size onto the sample. Video imaging of the sample under laser illumination allowed precise location of the focused laser beam on the sample. The Raman scattered light was collected in backscattering geometry and focused on the entrance slit of a LabRamHR UV spectrometer with 600 g/mm gratings. The confocal hole was maintained at 100 μm and the scattered light was then dispersed onto an air-cooled, 1024 × 256 CCD detector. The Raman signal was averaged for a minimum of 30 s at each location. Spectral maps were collected at 2.0–0.5 μm grid. Isolating characteristic peaks of Mg-carbonates and silicates allowed images of the spatial distribution of these phases to be created. The peak positions of the resulting Raman spectra were analyzed using a commercially available software package, GRAMS/32 or LabSpec data acquisition and analysis software.

The bulk powder XRD analyses were carried out on a Philips X'Pert MPD system with a vertical goniometer. The X-ray source is a long-fine-focus, ceramic X-ray tube with Cu anode.

3. RESULTS AND DISCUSSION

Bulk XRD analysis of the samples reacted at 35 °C for 14 days (Fig. 3) shows the presence of nesquehonite indicated by the characteristic reflections at d spacings of 6.480 Å (13.6° 2θ) and 2.617 Å (34.2° 2θ). The formation of nesquehonite is not unexpected owing to its rapid kinetics of precipitation. However, the XRD analysis also shows clear evidence for the formation of magnesite indicated by the d spacing reflections at 2.104 Å (42.8° 2θ) and 1.701 Å (53.5° 2θ). Although magnesite is expected to be thermodynamically stable, its formation is surprising given its well-known slow rate of precipitation at low temperatures (Oelkers et al., 2008; Saldi et al., 2009). There is also evidence for the formation of small amounts of dypingite indicated by reflections at d spacings of 10.80 Å (8.1° 2θ) and 5.890 Å (14.5° 2θ). At 50 °C XRD analysis shows that the dominant crystalline magnesium carbonate phase is clearly magnesite with small amounts of unreacted forsterite (Fig. 3). There is no evidence for the presence of either nesquehonite or dypingite based on the XRD analysis.

The ^{13}C NMR analysis of these samples, see Fig. 4, offers additional insight into the reaction products that formed during the 14 day experiments. The horizontally expanded spectral range (from 150 to 180 ppm) shows metal carbonate reaction products associated with ^{13}C SP-MAS spectra of forsterite reacted at 35 °C (Fig. 4a) and 50 °C (Fig. 4b). Their corresponding best simulated spectra are also shown at the right side of Fig. 4. Five peaks at 163.6 (peak 1), 165.3 (peak 2), 165.6 (peak 3), 168.8 (peak 4) and 170.2 (peak 5) ppm are required to fit the spectrum at 35 °C while four peaks at 163.5 (peak 1), 165.4 (peak 2), 169.0 (peak 4) and 170.0 (peak 5) ppm are needed to fit the spectrum at 50 °C. The peak centers of 165.3 (peak 2) and 165.6 (peak 3) in Fig. 4a are so close that their origins can be attributed to minor differences in crystal structures of the same species. The normalized peak areas based on per unit weight of sample and per unit number of accumulations are summarized in Table 1. Spectra acquired on magnesium carbonate standard minerals, i.e., nesquehonite, hydromagnesite and dypingite are included in Fig. 4 for aiding spectral assignments. Although each of the three standard minerals has two peaks that are near 163.6 and 165.3 ppm, only the peaks from nesquehonite closely match peak positions and relative peak intensities observed in reacted samples (Fig. 4a and b). Thus, the peaks located at 163.5 ± 0.1 ppm, 165.3 ± 0.1 ppm and 165.6 ppm in Fig. 4a and b can be assigned to nesquehonite with confidence. The peak observed at 170 ppm is assigned to $MgCO_3$, magnesite (Kwak et al., 2011). The peak at about 169 ppm (peak 4) is apparently a transient state between $MgCO_3$ and hydrate/hydroxylated $MgCO_3$ based on the fact that 169 ppm peak is between $MgCO_3$ and the nesquehonite, hydromagnesite and dypingite peaks.

The ^{1}H–^{29}Si CP-MAS NMR spectra given in Fig. 5 supports the transition state assignment. The 169 ppm peak (Fig. 5, peak 4) is significantly enhanced relative to the 170 ppm peak (peak 5) in the CP spectra (Fig. 5) compared with their counterparts in the SP-MAS spectra (Fig. 4a and b), indicating there are more protons associated with either H_2O or –OH groups for the 169 ppm peak than that for the 170 ppm peak. The fact that the 170 ppm peak is detectable in the ^{1}H–^{29}Si CP-MAS NMR spectra indicates that the $MgCO_3$ particle size must be small so that a part of the carbon is close to the surface and interacting with surface protons, thus contributing to a CP signal.

Based on the NMR analysis (Fig. 4 and Table 1) we conclude that nesquehonite is the major metal carbonation product, accounting for about 83% of the total metal carbonates at 35 °C. The NMR results also show that even at temperatures as low as 35 °C, an appreciable amount of anhydrous magnesite (~18%) is formed during 14 days of reaction time. At a reaction temperature of 50 °C, magnesite becomes the dominant metal carbonate product (~67%). The overall NMR results thus strongly support the bulk XRD analysis in confirming the presence of magnesite at both 35 °C and 50 °C.

It is also interesting to note that the relative ratio of the total metal carbonate product at 35 °C versus that at 50 °C, i.e., 0.849 determined from ^{13}C SP-MAS experiments, is

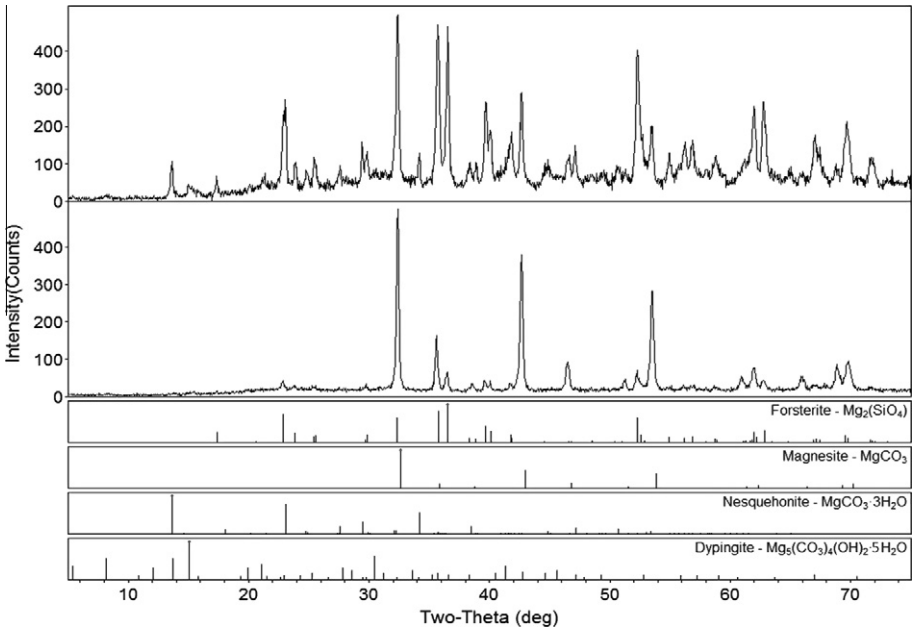

Fig. 3. XRD analysis of the 14 day forsterite reaction products. Top 35 °C. Bottom 50 °C.

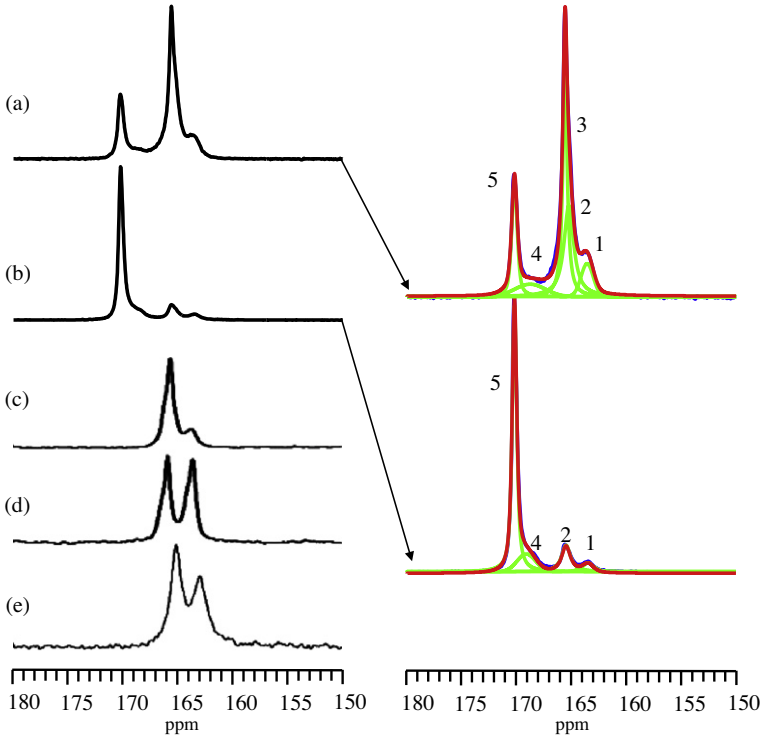

Fig. 4. ^{13}C SP-MAS spectra of 0.5 g nano-Mg_2SiO_4 + 90 atm CO_2 + 0.5 g H_2O (not in contact with mineral) reacted for 14 days at 35 °C (a) and 50 °C (b), respectively. ^{13}C SP-MAS spectra were acquired using an accumulation number of 8616 (a) and 8548 (b), respectively. The absolute integrated peak intensity obtained from spectral deconvolution that is further normalized to unit sample weight is given in Table 1. The spectra of nesquehonite (c), hydromagnesite (d) and dypingite (e) are also included for comparison.

very close to that of 0.824 determined from ^{29}Si SP-MAS (see discussion below). This consistency implies that quantitative information can be obtained from both ^{29}Si SP-MAS and ^{13}C SP-MAS, offering a cross validation for the NMR results.

Experimental and the peak fitted/peak deconvoluted ^{29}Si MAS NMR spectra of nano-forsterite reacted with 90 atm CO_2 and saturated H_2O in $scCO_2$ for 14 days are shown in Fig. 6. Three peaks are observed with the bulk forsterite located at −61.6 ppm, silica Q3 at about −102

Table 1
The absolute peak areas of the various peaks in ^{13}C SP-MAS NMR spectra of forsterite normalized to per unit sample weight and per unit number of accumulations.

Peak	1	2	3	4	5
35 °C	163.6 ppm	165.3 ppm	165.6 ppm	168.8 ppm	170.2 ppm
	831 (9.5%)	2604 (29.7%)	2964 (33.8%)	764 (8.8%)	1609 (18.3%)
	Total peak area: 8772.347				
50 °C	163.5 ppm	165.4 ppm		169.0 ppm	170.0 ppm
	522 (5.0%)	1485 (14.4%)		1377 (13.3%)	6951 (67.3%)
	Total peak area: 10,334.6				

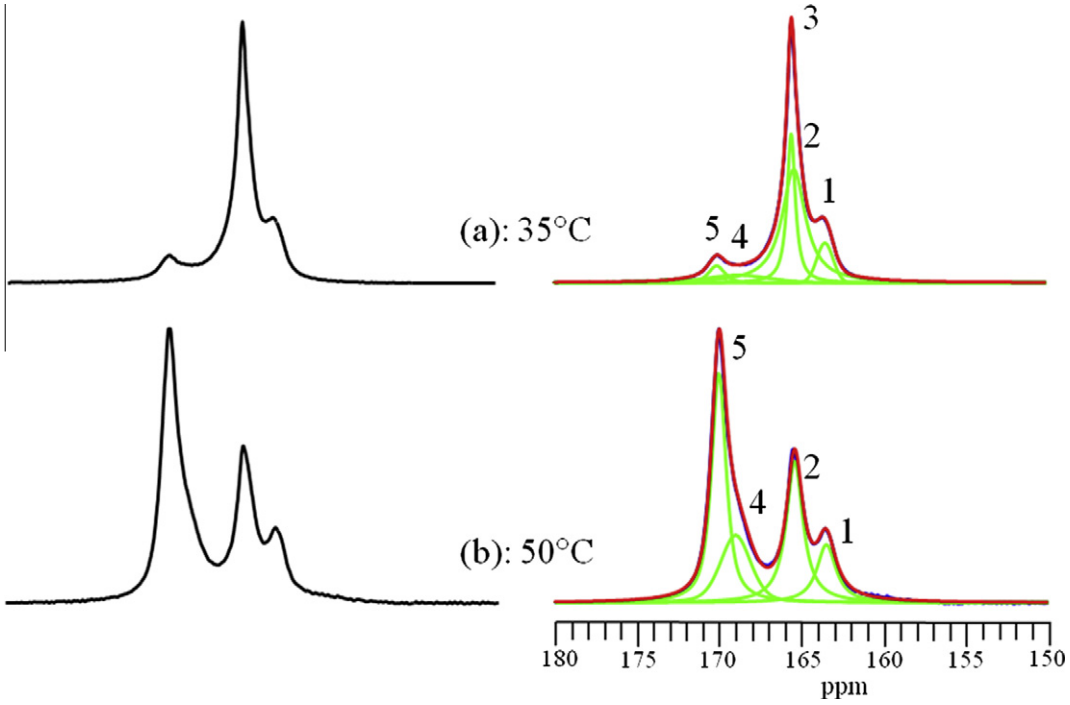

Fig. 5. ^{1}H–^{13}C CP-MAS spectra of Mg_2SiO_4 at 90 atm CO_2 reacted for 14 days at 35 °C (a) and 50 °C (b), respectively. These spectra were acquired using a sample spinning rate of 6 kHz, a contact time of 4 ms, a recycle delay time of 5s, and an accumulation number of 7980 (a) and 6860 (b), respectively.

and silica Q4 at about −111.5 ppm, respectively. These spectral assignments are based on our prior investigations (Kwak et al., 2011). Since the total number of silica atoms is conserved during the reaction, the percentage of forsterite reacted can be calculated as the peak area ratio of (Q3 + Q4)/(Mg_2SiO_4 + Q3 + Q4). At 35 °C about 77.6% of the original forsterite was converted to amorphous silicates while at 50 °C the conversion increased to 94.2%. Compared with the result at 35 °C, the conversion at 50 °C is accompanied by a significant increase in silica Q4 structure and a moderate decrease in silica Q3 structure based on absolute quantification of the ^{29}Si MAS spectrum scaled to per unit sample weight and per unit number of accumulation numbers. This result indicates the formation of a more anhydrous SiO_2 structure at increasing temperature. Since each Q3 structure contains one Si–OH and is exclusively at the silicate surface, the existence of a significant Q3 structure at both 35 °C (36.2%) and 50 °C (26.5%) means the amorphous silicate structure is either highly porous or the corresponding particle size is very small with a significant amount of Si at the surface. Thus, it can be concluded that the amorphous silicate structure associated with the reacted forsterite must be highly porous.

Raman spectra of the Mg-carbonate phases magnesite, dypingite, hydromagnesite, and nesquehonite share many similarities due to the intense signal from the molecular vibrations of the CO_3^{2-} group and are quite distinct from the Raman spectrum of forsterite. Therefore evidence of conversion of forsterite to Mg-carbonate is readily obtained from Raman spectral mapping of the individual reacted forsterite particles.

The dominant peak in the Mg-carbonate spectra is the symmetric stretch of the CO_3 group which varies from 1095 to 1125 cm^{-1} depending on the carbonate. Of the Mg-carbonates magnesite displays the most distinctive Raman spectrum with well-defined peaks at 209, 331, 738,

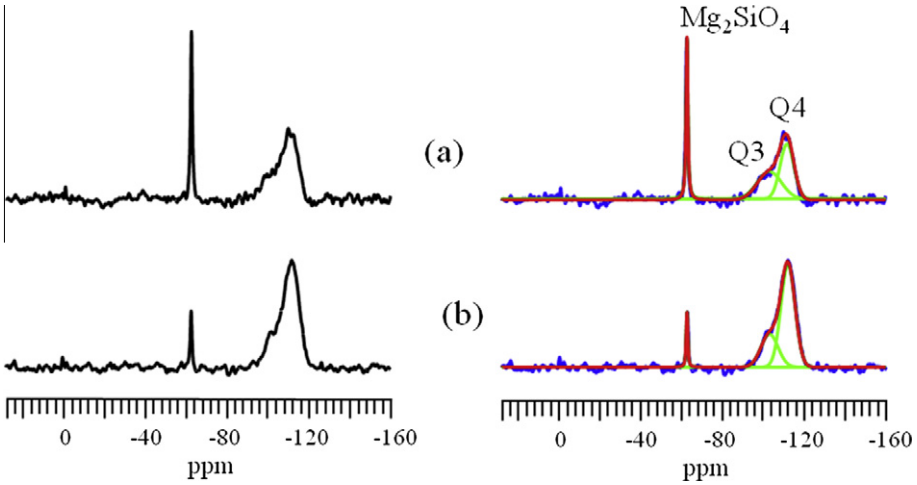

Fig. 6. ^{29}Si SP-MAS spectra of Mg_2SiO_4 at 90 atm CO_2 reacted for 14 days at 35 °C (a) and 50 °C (b), respectively. Peak assignments are −61.9 ppm (bulk Mg_2SiO_4), −102 ppm (silica Q3), and −111.6 ppm (silica Q4). ^{29}Si MAS spectra were acquired using an accumulation number of 12,788 (a) and 12,620 (b), respectively. The absolute integrated peak intensity obtained from spectral deconvolution that is further normalized to unit sample weight is given below. 35 °C: 140 (22.4%) Mg_2SiO_4; 226 (36.2%) silica Q3; 259 (41.4%) silica Q4. 50 °C: 41 (5.8%) Mg_2SiO_4; 187 (26.5%) silica Q3; 478 (67.7%) silica Q4.

1097 and 1410 cm^{-1} (Edwards et al., 2005). The Raman spectra of dypingite and hydromagnesite are nearly identical both having peaks at 150, 210, 732, 763, 1125, 1455 and 1527 cm^{-1} (Edwards et al., 2005). However, dypingite can be identified by a low intensity shoulder peak at 1090 cm^{-1}. The Raman spectrum of nesquehonite displays peaks at 187, 228, 703, 1099, 1419 and 1509 cm^{-1} (Hales et al., 2008; Hopkinson et al., 2008).

The majority of the Raman spectral maps of the larger aggregated (>100 μm) forsterite particles reacted for 14 days at 35 °C showed Raman spectra characteristic of forsterite with little evidence of carbonate reaction products. However several of the aggregates less than 50 μm in diameter showed spectral features of both forsterite and magnesite phases in varying proportions even on micron scale spatial resolution of the laser beam (Fig. 7a). We cannot be sure if the relationship between magnesite identification and particle size is as a result of a difference in particle reactivity or the fact that the Raman analysis was done after the NMR analysis. The NMR analysis required the particles to be packed tightly into the NMR cell which could have altered the particle sizes observed in the Raman spectroscopy.

Raman spectral maps of the forsterite aggregates less than 50 μm in diameter at 50 °C revealed particles with a marked increase in the predominance of magnesite (Fig. 7b).

Low resolution SEM images of the reacted forsterite at 35 °C, Fig. 8a, shows the original forsterite particles are partially covered by reaction products. A higher resolution image, Fig. 8b, reveals that the reaction products have different morphologies with several showing a cubic structure similar to that expected for magnesite (King et al., 2010). This is in agreement with the XRD, NMR and Raman results which clearly show the formation of magnesite in these low temperature samples.

SEM images of the surface of the reacted forsterite at 50 °C, Fig. 9, show the clear presence of cubic structures similar to what is expected for magnesite that almost entirely cover the original forsterite particles but also the presence of large micron-sized spherical precipitates with no known morphological relationship to magnesite. EDS analysis showed only Mg and O in the large spherical particles with no detectable silica. Morphologically, the particles appear identical to similar sized particles identified as nesquehonite by Wu et al. (2011), see Fig. 2d (Wu et al., 2011). Hence, although nesquehonite was identified at 50 °C by NMR and the particle morphology is representative of the possible forms of nesquehonite, the precipitates do not have long range crystalline order.

To further explore the range of conditions that might promote magnesite formation we conducted additional studies of the reactivity of forsterite in an in situ XRD reaction cell (7 days), for short time frames (84 h) using the Parr vessel with water-saturated $scCO_2$ as described above, and for 14 days of reaction in the Parr vessel used above except that water (0.1 g ~700% water saturation in $scCO_2$) was added directly to the stainless steel vial containing forsterite, rather than to the bottom of the reaction cell. In the latter case there is a small amount of aqueous solution in direct contact with the forsterite for the entire length of the experiment.

After 84 h of reaction in water-saturated $scCO_2$, bulk XRD analysis was unable to detect the presence of any crystalline phase other than forsterite. However, ^{13}C NMR, being much more sensitive, clearly shows the presence of small amounts of magnesite and nesquehonite (Fig. 10) even at these early reaction times. The NMR results suggest that the initial formation of magnesite must take place relatively soon after contact with the water-saturated $scCO_2$.

The results of the in situ XRD study, Fig. 11, after 7 days of reaction also show the clear presence of magnesite. In fact, magnesite is the most important crystalline phase reaction product in these 7 day experiments. Upon

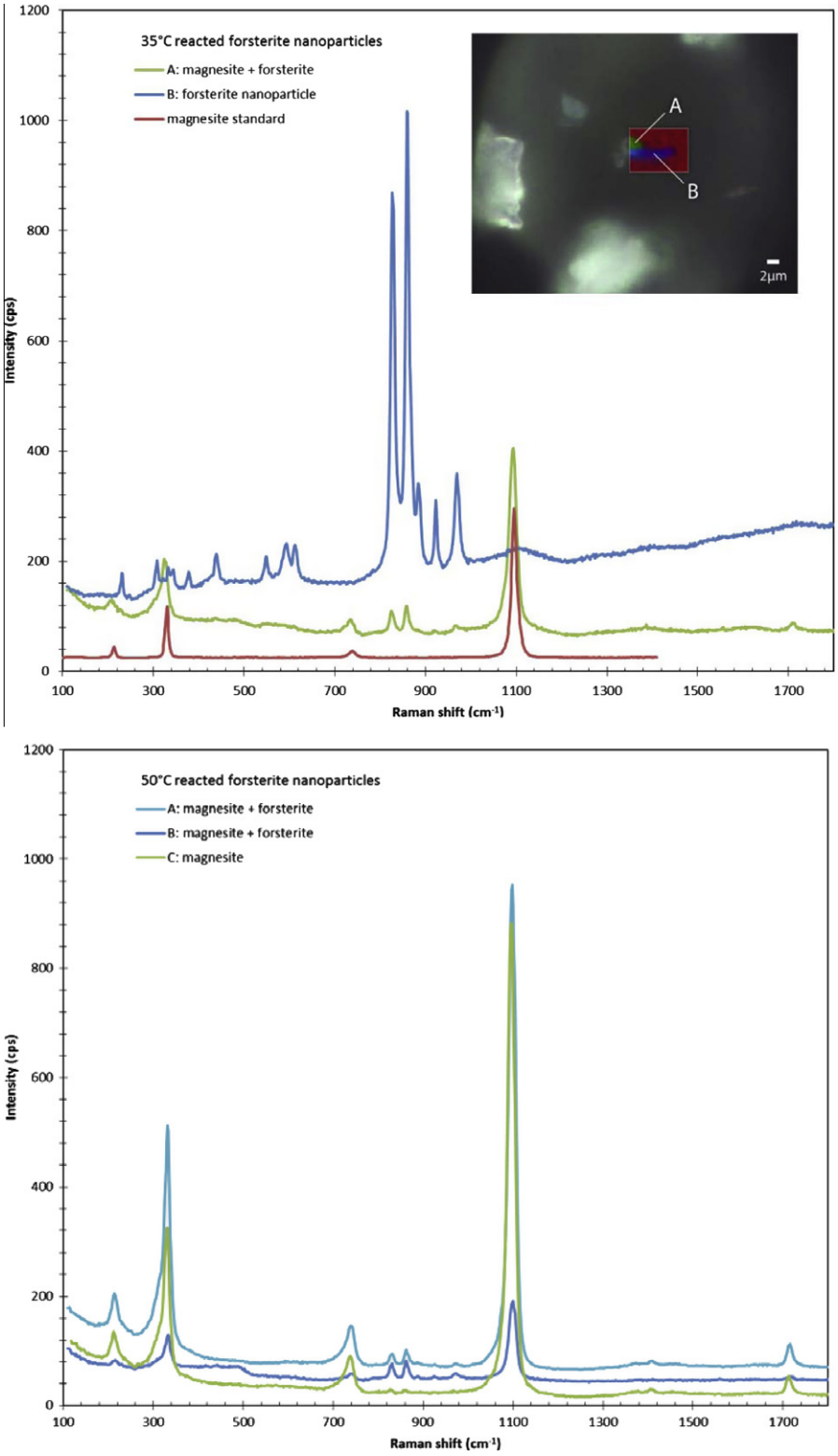

Fig. 7. Raman spectra of forsterite reacted for 14 days: (a) 35 °C, inset shows spectral map of a magnesite plus forsterite nodule (A) on an aggregate of forsterite nanoparticles (B); (b) 50 °C.

depressurization the intensity of the magnesite reflections increase, presumably as a result of the reduced interference of high pressure CO_2 as previously observed by Schaef et al. (2012). In addition to the magnesite reflections there is also a reflection at about 25.8° 2θ which does not match the pattern for magnesite. Though we cannot be sure, the closest

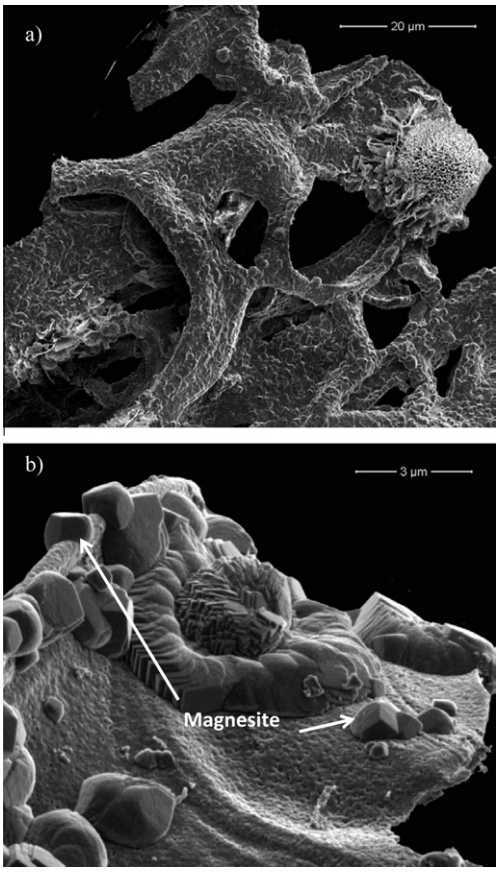

Fig. 8. SEM images of the reacted forsterite at water saturation at 35 °C and 90 atm pressure for 14 days (a) low resolution image showing the distribution of reaction products, (b) high resolution image illustrating the different morphologies of the surface precipitates. The cubic structures indicate the formation of magnesite. The other structures are presumably nesquehonite based upon the NMR, XRD, and Raman results.

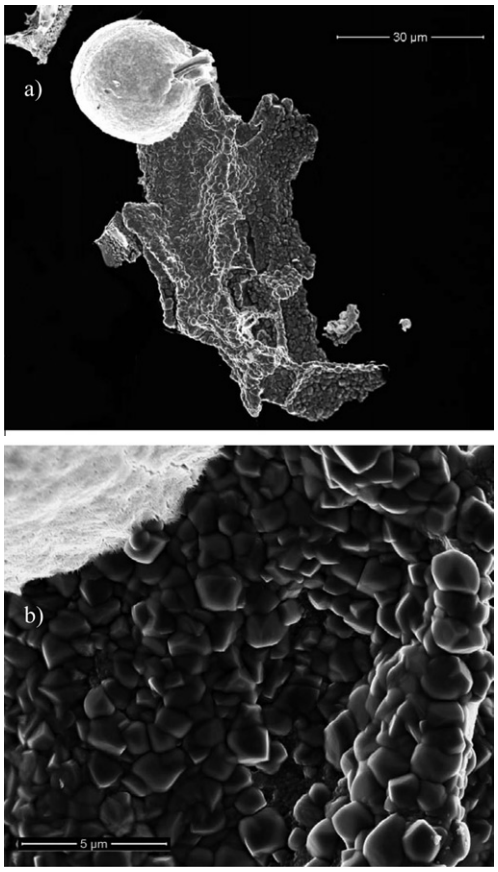

Fig. 9. SEM images of the reacted forsterite in water-saturated $scCO_2$ at 50 °C and 90 atm pressure for 14 days (a) low resolution image showing the morphologies of the reaction products and (b) high resolution illustrating the magnesite coverage of the original forsterite particles.

match to this peak appears to be the characteristic reflection for a crystalline silica hydrate originally reported by Eugster (1967). Interestingly, this peak disappears upon depressurization and must become amorphous, probably transforming to amorphous silica. In situ XRD also indicates that most of the original forsterite has been transformed to reaction products, in agreement with our 14 day experiments conducted in an entirely different apparatus and characterized under ex situ conditions. The fact that magnesite formation was verified by in situ measurements discounts the possibility that magnesite formed during sample cooling and depressurization prior to the ex situ analyses.

Bulk XRD ex situ analysis of our 14 day experiments with the nanoforsterite in direct contact with the initially added water also shows that the only crystalline reaction product is magnesite, with very little forsterite remaining. This result was confirmed by ^{13}C NMR spectroscopy which indicates as much as 95% of the magnesium carbonate reaction products consisted of magnesite. SEM analysis of these samples also showed the presence of small (~1 μm) cubic structures characteristic of magnesite, along with rod like particles indicating the formation of some nesquehonite along with magnesite.

4. CONCLUSIONS AND IMPLICATIONS

The forsterite used in this study is a high surface area material which reacts rapidly in the presence of water-saturated $scCO_2$. In fact, even after only 84 h of reaction there is clear evidence for the formation of magnesium carbonates including magnesite and nesquehonite by ^{13}C NMR spectroscopy. In situ XRD analysis after 7 days of reaction shows that the principal crystalline carbon-containing reaction product is magnesite. After 14 days of reaction, magnesite becomes a reaction product even at 35 °C and the primary crystalline reaction product at 50 °C. At 50 °C and 14 days of reaction essentially all of the forsterite has transformed to reaction products, either magnesite or a form of nesquehonite amorphous to X-rays. The presence of magnesite was verified by XRD, ^{13}C NMR spectroscopy, and Raman spectroscopy and the SEM images reveal the presence of cubic crystals with a morphology expected for magnesite. The silica phase appears to be a highly porous form of amorphous silica. No evidence is found for Si–O–Mg bonding in the silica reaction product.

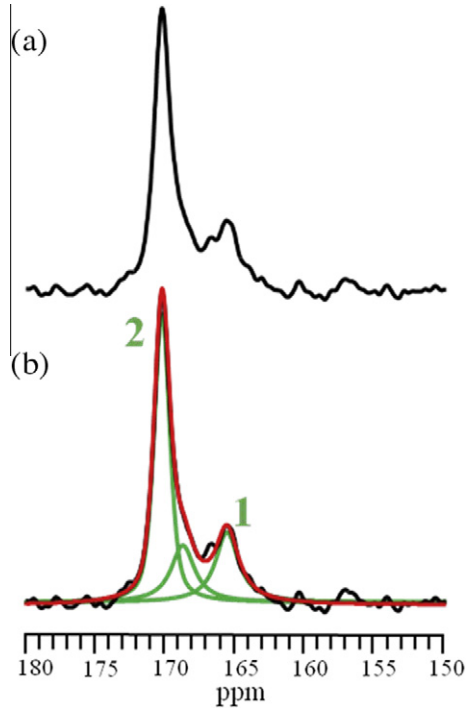

Fig. 10. ^{13}C MAS NMR spectrum of 8.5 mg nano-forsterite reacted with saturated H_2O in 90 atm of $scCO_2$ at 50 °C for 84 h. (a) Experimental spectrum; (b) Superimposed experimental (black) and fit (red) spectra along with the individual peaks used for generating the best fit. Peak assignments are **1**: 165.6 ppm (nesquehonite); **2**: 170.3 ppm (crystalline magnesite). Based on the total peak area, the percentage of forsterite reacted was about 7.8%. (For interpretation of the references to color in this figure legend, the reader is referred to the web version of this paper.)

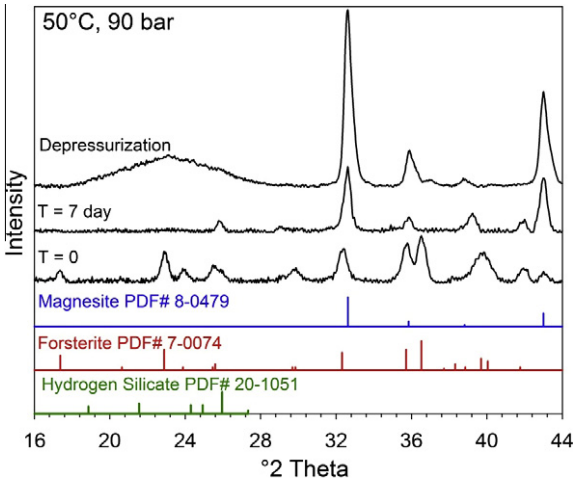

Fig. 11. In situ XRD analysis of forsterite reacted at 50 °C and 90 atm CO_2 pressure for 7 days.

The formation of magnesite at these lower temperatures is surprising and significant. Apparently, either mechanistic requirements for magnesite precipitation (e.g., Mg^{2+} dehydration) are uniquely met or the transformation of nesquehonite to magnesite is kinetically more favorable in these relatively low water content systems at high partial pressures of CO_2. In this regard, it appears that the nature of the water in contact with the reacting surface is a key factor in the enhanced formation of magnesite. It is also interesting that magnesite formation occurred both when excess water (over that required to saturate the $scCO_2$) was added directly to the forsterite samples and when water-saturated $scCO_2$ fluid came in contact with the forsterite samples. Regarding formation of water films on forsterite, Loring et al. (2011) have shown that the forsterite surface readily uptakes water even from $scCO_2$ fluids below water saturation. This uptake of water ostensibly forms a thin (few nm) water film coating the forsterite surface. The formation of a thin water film is also in agreement with recent molecular dynamics simulations (Kerisit et al., 2012) indicating that the strong affinity of water for the forsterite surface yields a film at least 3 water monolayers thick. This thin water film may provide unique conditions for magnesite growth, such as reducing the effective Mg^{2+} dehydration energy or facilitating the transformation of nesquehonite to magnesite, as compared to a more bulk-like aqueous solution. In any event, the observation of low temperature magnesite formation is a discovery with important implications for accurately predicting the long-term disposition of $scCO_2$ upon subsurface disposal.

This study further reinforces the importance of wet $scCO_2$ as a key reactive fluid phase in subsurface CO_2 reservoirs where mineral contact with this fluid will persist for decades. As previously discussed by Kwak et al. (2011), there is a water concentration threshold that marks the transition from initial hydrated reaction products to formation of anhydrous metal carbonates. This transformation can liberate water which maintains the forward reaction. In other words, once magnesite forms the reaction should, in principle, barring both transport limitations and formation of other water-consuming phases (e.g., Q3 silica species), proceed to completion, with H_2O acting as a catalyst. In the present experiments, water can be released from initially formed nesquehonite, reaction (2), a process previously observed to occur only at higher temperature (i.e., 80 °C; Kwak et al., 2011). The research reported here shows that magnesite can form in low water content $scCO_2$ systems at temperatures as low as 35 °C, which indicates that the impact of water recycling on mineral reactions is potentially important in a wide range of prospective CO_2 disposal reservoirs.

Finally, at present we do not believe that the enhanced formation of magnesite is solely as a result of the possibly lower activity of water in these systems. For example, at 35 °C we observe the formation of both nesquehonite and magnesite which are linked to the activity of water, reaction (2) above. However, using thermodynamic data from the review of Robie and Hemingway (1995) which is in good agreement with the data reported in Hanchen et al. (2008), gives a free energy change for reaction (2) of −15.4 kJ/mol at 35 °C (Robie and Hemingway, 1995). Such a strongly negative free energy change indicates that magnesite plus liquid water should be the stable phases at 35 °C relative to nesquehonite. Certainly, the effective water

activity at some time during the experiment could have been lower than the equilibrium value determined by this reaction, but in such an event the reaction should go even further to the right. Hence the presence of nesquehonite in this system is a clear indication of a lack of overall thermodynamic equilibrium. Determining precisely what the specific conditions are that promote magnesite formation at low temperature is the subject of on-going reach efforts at this laboratory.

ACKNOWLEDGMENT

We would like to thank Professor Alexandra Navrotsky at the University of California, Davis for supplying the initial sample of nanoforsterite and Dr. John S. Loring at Pacific Northwest National Laboratory (PNNL) for his assistance in subsequent nanoforsterite synthesis. We also would like to thank Dr. François Guyot, Professor John Kasuba, Dr. Eric Oelkers, and an anonymous reviewer for their helpful suggestions to improve this manuscript. Thanks also go to Dr. Mark Bowden for performing TOPAS refinement on the nanoforsterite XRD pattern. This work was supported by the U.S. Department of Energy (DOE), Office of Basic Energy Sciences through a Single Investigator Small Group Research (SISGR) grant at Pacific Northwest National Laboratory (PNNL). Several of the experiments were performed using EMSL, the Environmental Molecular Sciences Laboratory, a national scientific user facility sponsored by the Department of Energy's DOE Office of Biological and Environmental Research, and located at PNNL. PNNL is operated for DOE by Battelle Memorial Institute under Contract# DE-AC06-76RLO-1830.

REFERENCES

Angus S., Armstrong B. and De Reuck K. M. (1976) International thermodynamic tables of the fluid state. In *Carbon Dioxide*, vol. 3. Pergamon, Oxford, New York.

Bachu S. (2002) Sequestration of CO_2 in geological media in response to climate change: Road map for site selection using the transform of the geological space into the CO_2 phase space. *Energy Convers. Manage.* **43**, 87–102.

Bachu S. (2008) CO_2 storage in geological media: Role, means, status and barriers to deployment. *Prog. Energy Combust. Sci.* **34**, 254–273.

Bachu S. and Adams J. J. (2003) Sequestration of CO_2 in geological media in response to climate change: Capacity of deep saline aquifers to sequester CO_2 in solution. *Energy Convers. Manage.* **44**, 3151–3175.

Benson S. M. and Surles T. (2006) Carbon dioxide capture and storage: An overview with emphasis on capture and storage in deep geological formations. *Proc. IEEE* **94**, 1795–1805.

Chen S. S. and Navrotsky A. (2010) Calorimetric study of the surface energy of forsterite. *Am. Mineral.* **95**, 112–117.

Daval D., Sissmann O., Menguy N., Saldi G. D., Guyot F., Martinez I., Corvisier J., Garcia B., Machouk I., Knauss K. G. and Hellmann R. (2011) Influence of amorphous silica layer formation on the dissolution rate of olivine at 90 °C and elevated pCO_2. *Chem. Geol.* **284**, 193–209.

Deelman J. C. (1999) Low-temperature nucleation of magnesite and dolomite. *Neues Jb. Mineral. Monat.*, 289–302.

Edwards H. G. M., Villar S. E. J., Jehlicka J. and Munshi T. (2005) FT-Raman spectroscopic study of calcium-rich and magnesium-rich carbonate minerals. *Spectrochim. Acta A – Mol. Biomol. Spectrosc.* **61**, 2273–2280.

Eugster H. P. (1967) Hydrous sodium silicates from Lake Magadi Kenya – Precursors of bedded chert. *Science* **157**, 1177.

Garcia B., Beaumont V., Perfetti E., Rouchon V., Blanchet D., Oger P., Dromart G., Huc A. Y. and Haeseler F. (2010) Experiments and geochemical modelling of CO_2 sequestration by olivine: Potential, quantification. *Appl. Geochem.* **25**, 1383–1396.

Giammar D. E., Bruant R. G. and Peters C. A. (2005) Forsterite dissolution and magnesite precipitation at conditions relevant for deep saline aquifer storage and sequestration of carbon dioxide. *Chem. Geol.* **217**, 257–276.

Guyot F., Daval D., Dupraz S., Martinez I., Menez B. and Sissmann O. (2011) CO_2 geological storage: The environmental mineralogy perspective. *C.R. Geosci.* **343**, 246–259.

Hales M. C., Frost R. L. and Martens W. N. (2008) Thermo-Raman spectroscopy of synthetic nesquehonite – Implication for the geosequestration of greenhouse gases. *J. Raman Spectrosc.* **39**, 1141–1149.

Hanchen M., Prigiobbe V., Storti G., Seward T. M. and Mazzotti M. (2006) Dissolution kinetics of fosteritic olivine at 90–150 °C including effects of the presence of CO_2. *Geochim. Cosmochim. Acta* **70**, 4403–4416.

Hanchen M., Prigiobbe V., Baciocchi R. and Mazzotti M. (2008) Precipitation in the Mg-carbonate system – Effects of temperature and CO_2 pressure. *Chem. Eng. Sci.* **63**, 1012–1028.

Hayashi S. and Hayamizu K. (1991) Chemical shift standards in high-resolution solid-state NMR (1) ^{13}C, ^{29}Si, and ^{1}H nuclei. *Bull. Chem. Soc. Jpn.* **64**, 685–687.

Hopkinson L., Rutt K. and Cressey G. (2008) The transformation of nesquehonite to hydromagnesite in the system CaO–MgO–H_2O–CO_2: An experimental spectroscopic study. *J. Geol.* **116**, 387–400.

Kaszuba J. P., Janecky D. R. and Snow M. G. (2003) Carbon dioxide reaction processes in a model brine aquifer at 200 °C and 200 bars: Implications for geologic sequestration of carbon. *Appl. Geochem.* **18**, 1065–1080.

Kaszuba J. P., Janecky D. R. and Snow M. G. (2005) Experimental evaluation of mixed fluid reactions between supercritical carbon dioxide and NaCl brine: Relevance to the integrity of a geologic carbon repository. *Chem. Geol.* **217**, 277–293.

Kerisit S., Weare J. H. and Felmy A. R. (2012) Structure and dynamics of forsterite-scCO_2/H_2O interfaces as a function of water content. *Geochim. Cosmochim. Acta* **84**, 137–151.

King H. E., Plumper O. and Putnis A. (2010) Effect of secondary phase formation on the carbonation of olivine. *Environ. Sci. Technol.* **44**, 6503–6509.

Kwak J. H., Hu J. Z., Hoyt D. W., Sears J. A., Wang C. M., Rosso K. M. and Felmy A. R. (2010) Metal carbonation of forsterite in supercritical CO_2 and H_2O using solid state ^{29}Si, ^{13}C NMR spectroscopy. *J. Phys. Chem. C* **114**, 4126–4134.

Kwak J. H., Hu J. Z., Turcu R. V. F., Rosso K. M., Ilton E. S., Wang C., Sears J. A., Engelhard M. H., Felmy A. R. and Hoyt D. W. (2011) The role of H_2O in the carbonation of forsterite in supercritical CO_2. *Int. J. Greenhouse Gas Control* **5**, 1081–1092.

Lin H., Fujii T., Takisawa R., Takahashi T. and Hashida T. (2008) Experimental evaluation of interactions in supercritical CO_2/water/rock minerals system under geologic CO_2 sequestration conditions. *J. Mater. Sci.* **43**, 2307–2315.

Loring J. S., Thompson C. J., Wang Z., Joly A. G., Sklarew D. S., Schaef H. T., Ilton E. S., Rosso K. M. and Felmy A. R. (2011) In situ infrared spectroscopic study of forsterite carbonation in wet supercritical CO_2. *Environ. Sci. Technol.* **45**, 6204–6210.

McGrail B. P., Schaef H. T., Glezakou V. A., Dang L. X. and Owen A. T. (2009) Water reactivity in the liquid and supercritical CO_2 phase: Has half the story been neglected? *Energy Procedia* **1**, 3415–3419.

McPherson B. (2006) *Southwest Regional Partnership on Carbon Sequestration: Final Report – DE-PS26-03NT41983*. Socorro, New Mexico.

Nordbotten J. M. and Celia M. A. (2006) Similarity solutions for fluid injection into confined aquifers. *J. Fluid Mech.* **561**, 307–327.

Oelkers E. H., Gislason S. R. and Matter J. (2008) Mineral carbonation of CO_2. *Elements* **4**, 333–337.

Prigiobbe V., Costa G., Baciocchi R., Hanchen M. and Mazzotti M. (2009) The effect of CO_2 and salinity on olivine dissolution kinetics at 120 °C. *Chem. Eng. Sci.* **64**, 3510–3515.

Pruess K., Xu T. F., Apps J. and Garcia J. (2003) Numerical modeling of aquifer disposal of CO_2. *Spe Journal* **8**, 49–60.

Regnault O., Lagneau V., Catalette H. and Schneider H. (2005) Experimental study of pure mineral phases/supercritical CO_2 reactivity. Implications for geological CO_2 sequestration. *C.R. Geosci.* **337**, 1331–1339.

Robie R. A. and Hemingway B. S. (1995) *Thermodynamic Properties of Minerals and Related Substances at 298.15 K and 1 bar (105 pascals) Pressure and at Higher Temperatures*. U.S. Geological Survey, Denver, CO.

Saberi A., Alinejad B., Negahdari Z., Kazemi F. and Almasi A. (2007) A novel method to low temperature synthesis of nanocrystalline forsterite. *Mater. Res. Bull.* **42**, 666–673.

Saldi G. D., Jordan G., Schott J. and Oelkers E. H. (2009) Magnesite growth rates as a function of temperature and saturation state. *Geochim. Cosmochim. Acta* **73**, 5646–5657.

Schaef H. T., Windisch C. F., McGrail B. P., Martin P. F. and Rosso K. M. (2011) Brucite $Mg(OH_2)$ carbonation in wet supercritical CO_2: An in situ high pressure X-ray diffraction study. *Geochim. Cosmochim. Acta* **75**, 7458–7471.

Schaef H. T., Ilton E. S., Qafoku O., Martin P. F., Felmy A. R. and Rosso K. M. (2012) In situ XRD study of Ca^{2+} saturated montmorillonite (STX-1) exposed to anhydrous and wet supercritical carbon dioxide. *Int. J. Greenhouse Gas Control* **6**, 220–229.

Spycher N., Pruess K. and Ennis-King J. (2003) CO_2–H_2O mixtures in the geological sequestration of CO_2. I. Assessment and calculation of mutual solubilities from 12 to 100 °C and up to 600 bar. *Geochim. Cosmochim. Acta* **67**, 3015–3031.

Suto Y., Liu L. H., Yamasaki N. and Hashida T. (2007) Initial behavior of granite in response to injection of CO_2-saturated fluid. *Appl. Geochem.* **22**, 202–218.

Wu X. M., Cao H. Q., Yin G., Yin J. F., Lu Y. X. and Li B. J. (2011) $MgCO_3{\cdot}3H_2O$ and MgO complex nanostructures: Controllable biomimetic fabrication and physical chemical properties. *Phys. Chem. Chem. Phys.* **13**, 5047–5052.

Xu T. F., Apps J. A., Pruess K. and Yamamoto H. (2007) Numerical modeling of injection and mineral trapping of CO_2 with H_2S and SO_2 in a sandstone formation. *Chem. Geol.* **242**, 319–346.

Associate editor: Dimitri A. Sverjensky